Effects of Chemical Composition and Solidification Rate on the Solidification Behavior of High Cr White Irons

Hee Young Son , In Yong Jung , Baig Gyu Choi , Jong-Ho Shin , Chang-Yong Jo * , Je-Hyun Lee *

Posted Date: 1 February 2024

doi: 10.20944/preprints202402.0086.v1

Keywords: high-Cr white iron; primary austenite dendrite; M7C3/austenite eutectic structure; directional solidification; dendritic solidification; cellular solidification; in-situ composite; M23C6 carbide

Article

Effects of Chemical Composition and Solidification Rate on the Solidification Behavior of High-Cr White Irons

Hee Young Son [1,2], In Yong Jung [3], Baig Gyu Choi [3], Jong Ho Shin [4], Chang Yong Jo [1,*] and Je Hyun Lee [1*]

[1] Department of Advanced Materials, Changwon National University. 20, Changwon 51140, Republic of Korea; cyj20@changwon.ac.kr; ljh@changwon.ac.kr
[2] KPCM, Gyeongsan 38412, Republic of Korea; hyson@kpccorp.co.kr
[3] High Temperature Materials Department, Korea Institute of Materials Science, Changwon 51508, Korea; human3944@kims.re.kr; choibg@kims.re.kr
[4] Doosan Enerbility. 22 Doosanvolvo-ro Seongsan-gu, Changwon-si, Gyeongsangnam-do, Republic of Korea; jongho.shin@doosan.com
* Correspondence: cyj20@changwon.ac.kr (C.Y.Jo) and ljh@changwon.ac.kr (J.H.Lee); Tel.:+82-55-213-3695 (J.H. Lee)

Abstract: The effects of chemical composition and solidification rate on the solidification behavior of high-Cr white irons were investigated through directional solidification. Increasing the solidification rate in hypoeutectic alloys caused the finer dendrite arm spacing as expected. The eutectic structure which formed in the interdendritic region comprised of M_7C_3 and austenite, however, secondary dendrite arms of hypoeutectic alloys contained a few M_7C_3 particles that solidified prior to the eutectic structure. The transition from cellular to dendritic solidification occurred at a solidification rate between 50 μm/s and 100 μm/s in a near eutectic alloy. In the near eutectic alloy with cellular solidification, a directionally arrayed in-situ composite of M_7C_3/austenite formed within the cell. Speckle-like feature appeared in the intercellular region due to $M_{23}C_6$ carbide precipitation during subsequent cooling after freezing. Like dendrite arm spacing in hypoeutectic alloys, the inter-speckle spacing and the inter-fibre spacing became finer with increasing solidification rate in the cellular solidification range.

Keywords: high-Cr white iron; primary austenite dendrite; M_7C_3/austenite eutectic structure; directional solidification; dendritic solidification; cellular solidification; in-situ composite; $M_{23}C_6$ carbide

1. Introduction

High-Cr white irons which are applied to the wear resisting components, typically have a microstructure that consists of a martensitic or austenitic matrix and M_7C_3 carbide, which depends on the section size and chemical composition [1–3]. The phase fractions of the as-cast microstructure are dependent on chemical composition, especially C and Cr [2,3]. It is well known that the solidification of hypoeutectic high-Cr white irons begins with the formation of primary austenite dendrites, followed by the M_7C_3/austenite eutectic reaction [1–4]. During heat treatment of the alloys, the matrix becomes mainly martensitic, and $M_{23}C_6$ carbide precipitation occurs [2,3]. The excellent wear resistance of high-Cr white irons is attributed to the hard martensitic matrix and these carbides.

Not only does the chemical composition but also the casting variables have a strong influence on the cast microstructure of metallic alloys. Morphology and size of the existing phases of the alloys are closely related to casting variables. For instance, dendrite arm spacing and size of existing phases in the cast alloys are governed by solidification rate and thermal gradient during solidification [5]. It is well known that dendrite morphology and heat treatment cycle of the alloy are closely related to the mechanical properties [5].

 doi:10.20944/preprints202402.0086.v1

As mentioned in the previous study [6], the casting variable in conventional casting is the pouring temperature. It is not easy to measure the solidification rate or thermal gradient at the solid/liquid interface in conventional casting. Thus, the control of solidification variables during conventional casting of a given chemical composition is not available, except for pouring temperature. However, directional solidification (DS) allows for control of the solidification variables by regulating the withdrawal rate from the furnace and thermal gradient at the solid/liquid interface (G_L). The control of solidification variables in high-Cr white irons can develop various microstructures of a certain composition [6]. As reported earlier [2,3], variation of chemical compositions in high-Cr white iron also generates various fractions of primary austenite and eutectic structure in conventional castings.

Based on previous results [2,3,6], it is possible to find the relationship among microstructural features, casting variables, and chemical compositions of high-Cr white irons. Therefore, in the present study, high-Cr white irons with four different chemical compositions were directionally solidified at various solidification rates to find the relationship between solidification rate and microstructural evolution. The development of microstructural features with various solidification rates for these four different high-Cr white irons was analyzed in comparison with JMatPro and Thermo-Calc predictions.

2. Experimental Procedure

High-Cr irons with four distinct chemical compositions were prepared by master alloy making and remelting, followed by pouring into Y-blocks as previously reported [2,3]. Chemical compositions of the alloys are provided in Table 1. Phase prediction was conducted using commercial software Thermo-Calc (Thermo-Calc 2019b) based on the Steels/Fe-Alloys (V.9.1) database DB TCFE9 to understand the phase evolution during cooling. Additionally, JMatPro (Version12) was used to predict the phase diagram of the alloys based on Thermotech Fe data.

Specimens for directional solidification were machined from the Y-blocks to 4.7mm diameter rod by electric wire discharging machining (EDM). The EDM-machined rods were mechanically polished with abrasive paper to remove any recast and oxidized layers at the surface. The rod was inserted into an alumina tube (ID 5mm x OD 8mm x L 700mm), and then installed in a Bridgman-type directional solidification furnace (DS furnace) by clamping the bottom with a cold finger.

The specimen in the DS furnace was heated to 1600°C for melting and soaked for 30 minutes for stabilization. Each specimen was then directionally solidified at a constant thermal gradient of 10K/mm and various withdrawal rates of 5, 25, 50, and 100 μm/s.

For optical microscopy (OM: Nikon/ECLIPSE MA200, Tokyo, Japan) and scanning electron microscopy (SEM: JEOL/JSM-IT500LV, Tokyo, Japan), conventionally cast and DS specimens were metallographically prepared and etched with Vilella's reagent consisting of 45 ml glycerol, 15 ml nitric acid, and 30 ml hydrochloric acid. Microscopic observations were carried out both on the sections parallel and transverse to the solidified direction. Specimens for transmission electron microscopy (TEM: JEOL JEM-2100F) were prepared by mechanical polishing to a thickness of 60 micrometers, followed by twin jet polishing (Struers TenuPol-5). The solution for twin jet thinning was 10% perchloric acid. The existing phases were identified by TEM selected diffraction pattern (SADP) analysis.

Table 1. Chemical compositions of the specimens (wt%).

Alloy	C	Si	Mn	Cr	Ni	Mo	Fe
2127	2.13	0.71	0.67	27.00	0.89	0.86	Bal
2427	2.43	0.68	0.70	27.06	0.86	0.85	Bal
2827	2.78	0.70	0.70	27.34	0.87	0.85	Bal
2124	2.12	0.66	0.65	24.05	0.85	0.86	Bal

 doi:10.20944/preprints202402.0086.v1

3. Results and Discussions

3.1. Phase Prediction of the Conventionally Cast Alloys

Figure 1 shows the microstructure of the alloys in the as-cast condition. As the carbon content increases, the fraction of primary austenite dendrite decreases while that of the eutectic structure increases, which is expected. Alloys 2124, 2127, and 2427 contain large volume primary austenite dendrites, whereas a little dendrite appears in alloy 2827. Based on the volume of primary austenite dendrites, 2124, 2127, and 2427 were classified into hypoeutectic alloys, whereas 2827 was classified as a near eutectic alloy. The Thermo-Calc prediction of the pseudo-binary phase diagram in Figure 2(a) shows that alloy 2827 is in the hypereutectic composition range, even though alloy 2827 has some fraction of primary austenite dendrite in the conventional casting. However, the JMatPro prediction in Figure 2(b) shows that all the alloys 2127 and 2427 are obviously in the hypoeutectic range, and alloy 2827 is in the near eutectic range. Moreover, the Thermo-Calc prediction shows that the solidification of 2127 begins with delta-ferrite formation, but the JMatPro prediction displays the leading phase of solidification is austenite, like the other hypoeutectic alloys. The microstructural features of the alloys in Figure 1 and JMatPro phase prediction in Figure 2 display the same results.

Generally, it is known that the solidification of hypoeutectic cast iron begins with austenite formation from the liquid, followed by eutectic reaction in the interdendritic regions. [1,7] The eutectic reactions are graphite with austenite in gray irons and carbide with austenite in white irons [1,7]. It is known that the eutectic carbide in high-Cr white iron is M_7C_3 [1–3]. The gray eutectic areas in Figure 1 are composed of M_7C_3 and austenite (or martensite). $M_{23}C_6$ carbide, which is a precipitation product during heat treatment or post-cooling after solidification, may also exist in high-Cr white irons [1,2,8,9]. The carbides in the alloys will be addressed in directionally solidified materials.

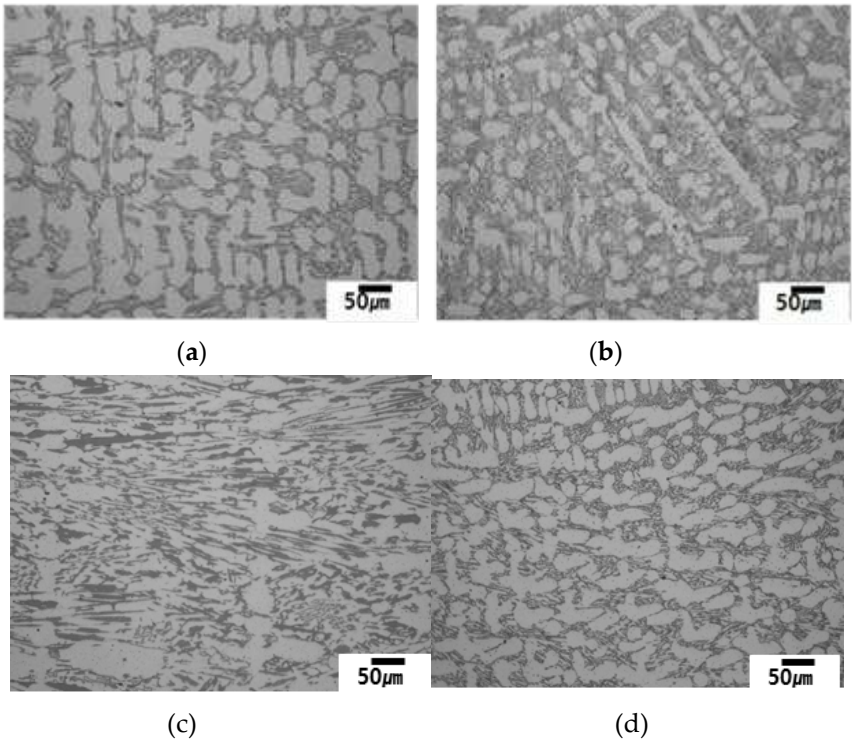

Figure 1. Optical micrographs of the conventionally cast alloys.: (a) 2127 (b) 2427 (c) 2827 (d) 2124.

Preprints.org (www.preprints.org) | NOT PEER-REVIEWED | Posted: 1 February 2024 doi:10.20944/preprints202402.0086.v1

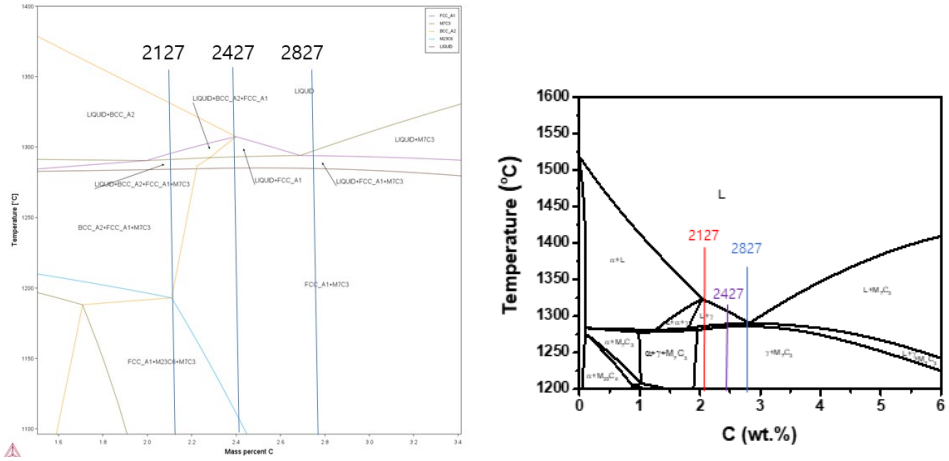

(a) (b)

Figure 2. Prediction of pseudo-binary phase diagram at constant Cr content of the alloys.: (a) Thermo-Calc ; (b) JMatPro.

3.2. Microstructure of the Directionally Solidified Alloys

Figure 1 shows that conventional casting produces an equiaxed microstructure with random orientation of existing phases. Pouring temperature is the only available casting parameter in conventional casting for a given configuration or mold, making it difficult to study the effect of casting or solidification variables. Directional solidification, which was developed for basic solidification studies and directional array, is useful for studying solidification behavior by controlling cooling rate (or solidification rate) or thermal gradient at the solid/liquid interface. In the present study, solidification behavior of the alloys was studied by directional solidification at various solidification rates at a constant thermal gradient of 10K/mm.

As mentioned above, the alloys 2124, 2127 and 2427 have a large volume of primary austenite dendrite in conventional castings, and the predicted phase diagram in Figure 2 also shows that the alloys are in the hypoeutectic composition range. However, the alloy 2827 is in the near eutectic composition range of hypoeutectic side. Thus, the directionally solidified alloys were classified into hypoeutectic alloys and a near-eutectic alloy based on microstructural analysis and JMatPro prediction.

3.2.1. Hypoeutectic Alloys with a Large Volume of Primary Austenite

Directional solidification for the alloys was carried out with solidification rates of 5, 25, 50, and 100 μm/s and at a constant thermal gradient of the solid/liquid interface of 10K/mm. As expected, primary austenite dendrite led the solidification, and final freezing occurred with the formation of M_7C_3/austenite eutectic structure in the interdendritic regions, both in conventional casting and directional solidification. Figures 3 and 4 display directionally solidified micrographs at each solidification rate for 2124, 2127 and 2427 alloys. As indicated in Figure 2, the alloys have hypoeutectic compositions far below the eutectic composition. Thus, a directional array of dendrites along the solidified direction is obvious at all solidification rates for the alloys, as shown in Figure 3. However, random orientation of dendrites appeared at the solidification rate of 100 μm/s. The existence of the randomly oriented dendrites means that the solidification condition is similar to that of equiaxed grains. The conventional equiaxed casting cooling rate (C) of the alloys might be calculated from the thermal gradient (G_L) and solidification rate (V_I). [10,11]

$$C = G_L V_I \quad (1)$$

where, G_L :10K/mm, V_I: 100 μm/s, pouring temperature 1600°C

 doi:10.20944/preprints202402.0086.v1

Even though it includes several experimental errors, the cooling rate of conventional casting for the alloys is calculated to be 10°C/s. The relatively faster solidification rate of 100 μm/s might cause more radiation cooling rather than conduction cooling to the cold finger.

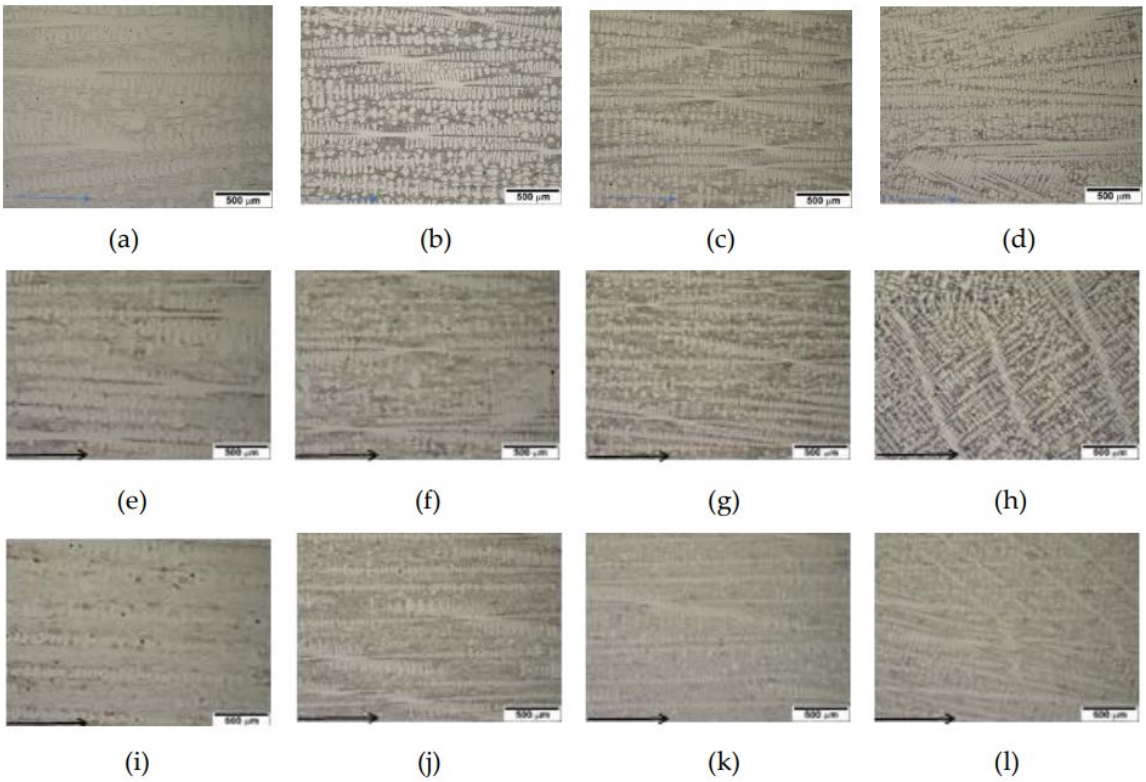

Figure 3. Micrographs parallel to the solidified direction at each solidification rate. Arrow shows solidified direction.: (a) 2124 at at 5 μm/s; (b) 2124 at 25 μm/s; (c) 2124 at 50 μm/s; (d) 2124 at 100μm/s; (e) 2127 at 5 μm/s; (f) 2127 at 25 μm/s; (g) 2127 at 50 μm/s; (h) 2127 at 100μm/s; (i) 2427 at 5 μm/s; (j) 2427 at 25 μm/s; (k) 2427 at 50 μm/s; (l) 2427 at 100μm/s.

In the transverse section to the solidified direction, well-developed secondary dendrite arms appeared clearly in Figure 4. The dendrite spacing becomes finer with increasing solidification rate in all alloys. The results are similar to the solidification behavior of Ni-base superalloys, which is generally accepted [10]. The well-aligned dendrite structure was caused by the preferred solidification of austenite, which means that the leading phase is austenite. The M_7C_3/austenite eutectic structure formed in the interdendritic regions where the final freezing occurred. The results show good agreement with Thermo-Calc predictions of solidification sequence [2,3] and those of JMatPro. The alloys have similar solidification behavior except for the difference in the amount of primary austenite dendrite.

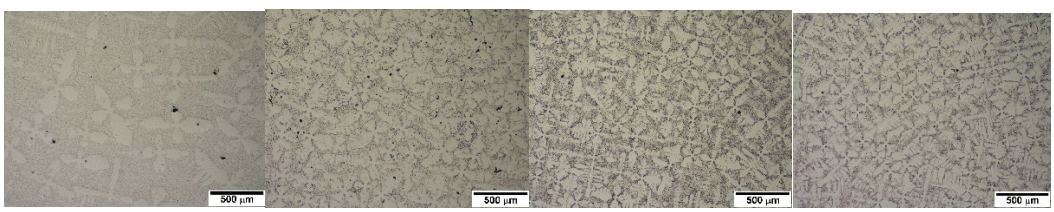

 doi:10.20944/preprints202402.0086.v1

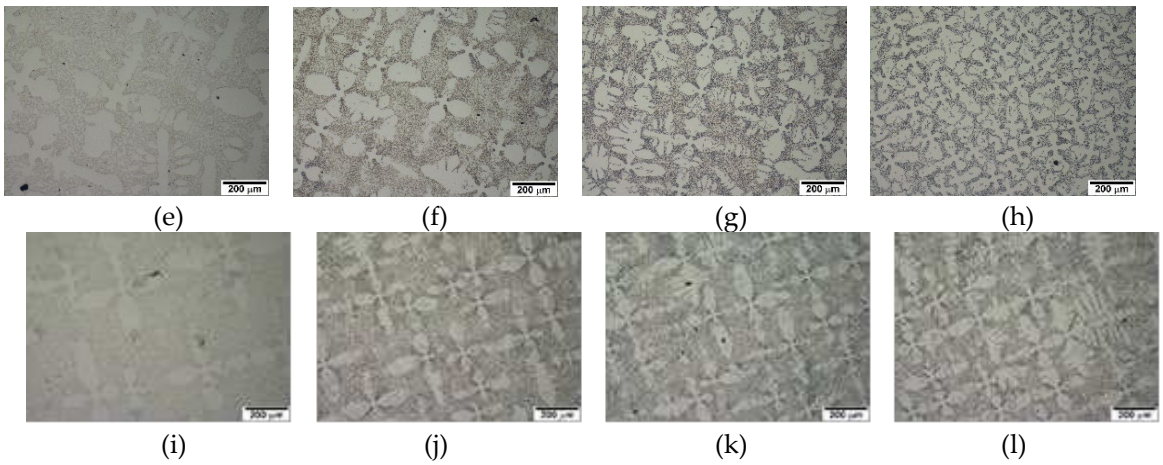

Figure 4. Micrographs transverse to the solidified direction at each solidification rate.: (a) 2124 at 5 µm/s; (b) 2124 at 25 µm/s; (c) 2124 at 50 µm/s; (d) 2124 at 100µm/s; (e) 2127 at 5 µm/s; (f) 2127 at 25 µm/s; (g) 2127 at 50 µm/s; (h) 2127 at 100µm/s; (i) 2427 at 5 µm/s; (j) 2427 at 25 µm/s; (k) 2427 at 50 µm/s; (l) 2427 at 100µm/s.

3.2.2. Directional Solidification of a Near Eutectic Alloy

As mentioned earlier, hypoeutectic alloys 2124, 2127 and 2427 contain a large amount of primary austenite dendrite that led solidification, and formation of M_7C_3/austenite eutectic structure in the interdendritic regions, as shown in Figure 4. On the other hand, the conventional castings of alloy 2827 contain small amount of primary austenite dendrite as shown in Figure 1c.

However, directional solidification with solidification variables may generate various microstructural features. The directionally solidified 2827 alloy shows that the microstructure varies with solidification rate, as displayed in Figure 5. A directional array of M_7C_3 carbide and austenite (referred as "in-situ composite" below) along the solidified direction is obvious at and below the solidification rate of 50 µm/s in Figure 5 (a)-(c), while primary austenite dendrite appears at the solidification rate of 100 µm/s in Figure 5 (d). The existence of randomly oriented dendrites at the solidification rate of 100 µm/s in 2827 alloy also was also caused by the same cooling rate calculated above (10°C/s).

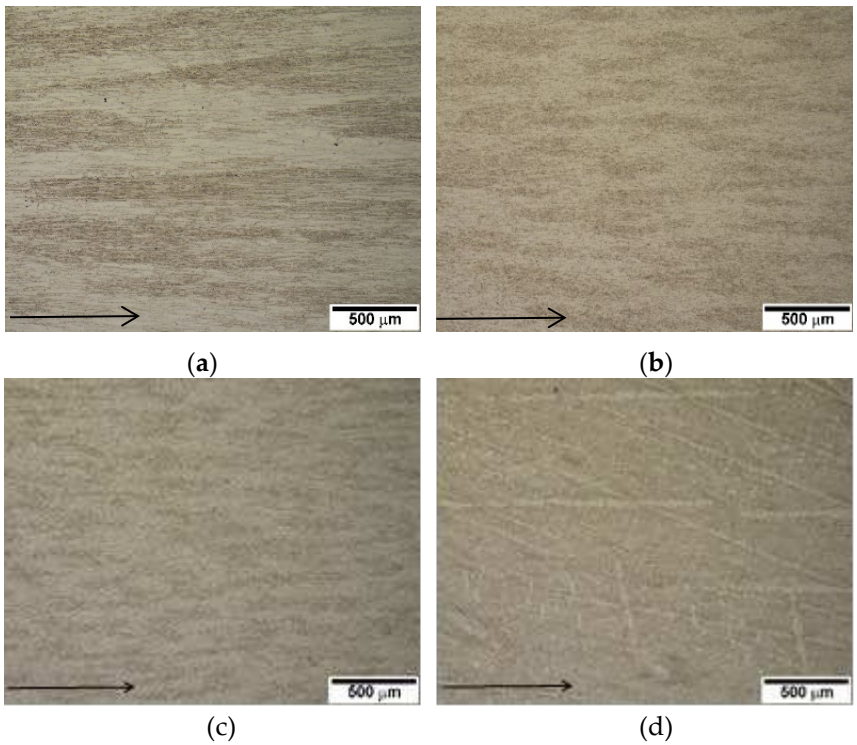

 doi:10.20944/preprints202402.0086.v1

Figure 5. Micrographs of 2827 alloy along the solidified direction at various solidification rates. Arrow shows solidified direction.: (a) 5 μm/s; (b) 25 μm/s; (c) 50 μm/s; (d) 100μm/s.

Figures 6a–c show SEM micrographs of the directional array of in-situ composite at and below the solidification rate of 50 μm/s, whereas Figure 6 (d) shows the coexistence of dendrite and M_7C_3/austenite eutectic structure at a solidification rate of 100 μm/s.

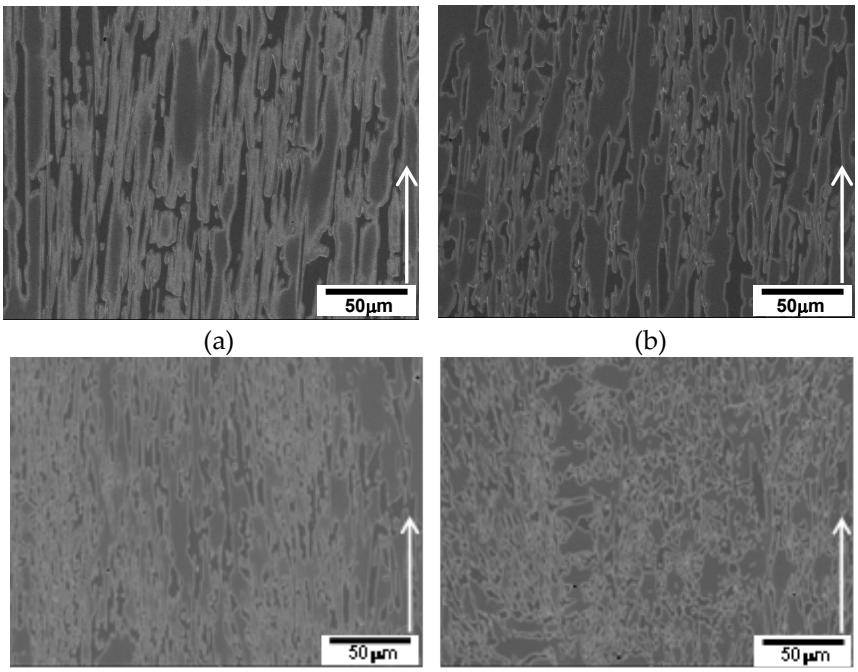

Figure 6. SEM micrographs of directionally solidified 2827 alloy showing in-situ composite at the solidification rates below 50 μm/s. Arrow indicates the solidified direction.: (a) 5 μm/s; (b) 25 μm/s; (c) 50 μm/s; (d) 100μm/s.

The inter-fibre spacing in the in-situ composite becomes finer with increasing solidification rate at and below μm/s as shown in Table 2. The transition of solidification behavior was observed between 50 μm/s and 100 μm/s, as seen in Figures 5 ~ 6. The micrographs transverse to the solidified direction in Figure 6 also demonstrate this transition, which is expected to be from cellular to dendritic solidification. The cellular solidification may have both relatively earlier and late freezing areas like the existence of interdendritic region and dendrite in dendritic solidification. The speckles (brown or gray) seen in Figures 7 (a) ~ 7 (c) transverse to the solidified direction are relatively later freezing areas during cellular solidification. Furthermore, the distribution and size of the speckles become uniform and finer with increasing solidification rate in Figures 7 (a) ~ 7 (c). Table 3 shows the measured inter-speckle spacing in 2827 alloy that becomes finer with increasing solidification rate at and below 50 μm/s.

Table 2. Measured inter-fibre spacing in 2827 alloy solidified at and below 50 μm/s.

solidification rate (μm/s)	5	25	50
inter-fibre spacing (μm)	6.6	6.0	4.0

 doi:10.20944/preprints202402.0086.v1

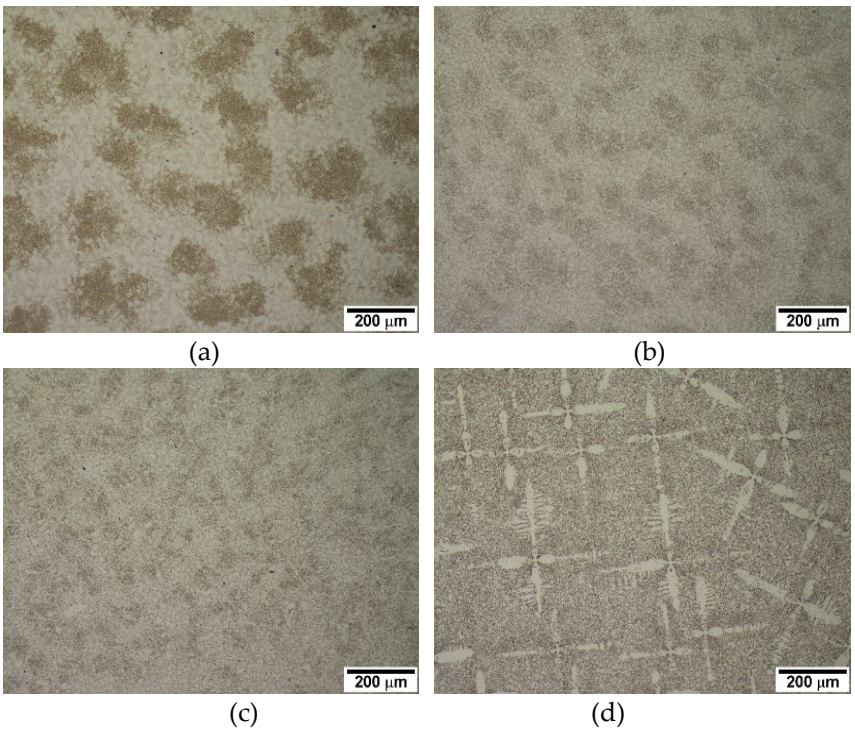

Figure 7. Micrographs of 2827 alloy transverse to the solidified direction at various solidification rates.: (a) 5 μm/s; (b) 25 μm/s; (c) 50 μm/s; (d) 100μm/s.

Table 3. Measured inter-speckle spacing in 2827 alloy solidified at and below 50 μm/s.

solidification rate (μm/s)	5	25	50
inter-speckle spacing (μm)	276	74.5	54.5

3.3. Solidification Behavior of the Alloys

Based on the microstructural observations discussed above, the solidification behavior of the alloys at different solidification rates has been categorized in Table 4. In hypoeutectic alloys, which are significantly below the eutectic composition, dendritic solidification was observed at relatively low solidification rates (~50 μm/s), with decreasing dendrite arm spacing as the solidification rate increased. However, at higher solidification rates (100 μm/s), the dendrite orientation became random. On the other hand, a transition from cellular to dendritic solidification was observed in a near-eutectic alloy (slightly away from the eutectic composition), occurring at a solidification rate between 50 μm/s and 100 μm/s in 2827 alloy.

The solidification behavior in directional solidification, specifically in hypoeutectic alloys with a negative slope of the liquidus m_L and solidus m_S, is influenced by various factors [10,11], including the thermal gradient at liquid G_L (Kmm/s), solidification rate V_I (mms-1), melting range ΔT (K), and diffusivity in liquid D_L (mm^2/s). Charlmer and Mclean proposed conditions for solidification behaviors in eq (2) to (4) [10,11]:

for the planar solidification;

$$G_L / V_I \geq -m_L C_o(1-k)/kD_L \quad (2)$$

$$= \Delta T / D_L \quad (3)$$

or for the cellular and dendritic solidification;

$$G_L / V_I < \Delta T / D_L \quad (4)$$

In eq (2), the condition for planar front solidification is presented, while eq (4) represents the condition for cellular or dendritic solidification. In eq (3)~(4), the G_L value comes from the furnace and has a constant value of 10K/mm in the present study. The V_I values range from 5 μm/s to 100

 doi:10.20944/preprints202402.0086.v1

μm/s for solidification rate, and each alloy has its own values of ΔT and D_L, which depend upon the alloy composition. Therefore, ΔT and D_L are constant values for each alloy, regardless of solidification rate. The ΔT value for each alloy can be measured using DSC thermal analysis or calculated using Thermo-Calc or JMatPro simulations. The calculated solidification data are listed in Table 5, but unfortunately, the DSC measurement was not successful.

For example, dendritic solidification occurred at all solidification rates in hypoeutectic alloys 2124, 2127 and 2427, which have a sufficient wide range of ΔT melting range, as listed in Table 5. Thus, the solidification conditions satisfied eq (3). Cellular solidification occurred at and below 50 μm/s solidification rates in 2827 alloy, and a transition from cellular to dendritic solidification appeared between 50-100 μm/s solidification rates. This may be attributed to the small melting range ΔT of the alloy compared to the other hypoeutectic alloys that have a large volume of primary dendrite, such as 2124, 2127 and 2427, which have a wide melting range, as shown in Table 5.

Table 4. Solidified feature of the alloys at each solidification rate.

Solidification rate / Alloy	5μm/s	25μm/s	50μm/s	100μm/s
2127	dendrite	dendrite	dendrite	Random oriented dendrite
2427	dendrite	dendrite	dendrite	Random oriented dendrite
2827	in-situ composite	in-situ composite	in-situ composite	Random oriented dendrite
2124	dendrite	dendrite	dendrite	Random oriented dendrite

Table 5. Thermo-Calc and JMatPro predictions on melting range of each phase (°C).

Alloy	T_l	T_E	T_{Ef}	⌀T(JMatPro) (T_l-T_s)	⌀T (Thermo-Calc) (T_l-T_s)
2127	1320	1287	1283	37	41
2427	1307	1289	1285	22	21
2827	1292	1290	1286	6	15
2124	1328	1290	1283	39	42

*where T_l: liquidus, T_s: solidus, T_E: eutectic begins, T_{Ef}: eutectic finishes.

3.4. Existing Microstructure

3.4.1. In-Situ Composite

As mentioned previously, an in-situ composite with a directional array along the solidified direction formed in the near eutectic alloy 2827 under specific conditions. The formation of the in-situ composite is related to a combination of the melting range and solidification rate, which are in turn linked to the alloy composition and solidification variables. The in-situ composite was observed only under cellular solidification conditions in the alloy, which had a large volume of eutectic structure in conventional castings. However, the hypoeutectic alloys 2124, 2127 and 2427 did not exhibit in-situ composite formation due to their relatively wide melting ranges, as shown in Table 5. Consequently, only dendritic solidification occurred in these alloys, as listed in Table 4.

 doi:10.20944/preprints202402.0086.v1

The micrographs of the in-situ composite in 2827 alloy display well-aligned M_7C_3/austenite along the solidified direction, as shown in Figure 6 (a)~(c). It is expected that the in-situ composite formed due to the competitive growth between M_7C_3 carbide and austenite within the cell. DSQ experiments revealed the competitive growth of M_7C_3 and austenite at cellular solidification condition of 50 μm/s in Figure 8 (a), whereas primary austenite dendrite leads the solidification at dendritic solidification condition of 100 μm/s in Figure 8 (b).

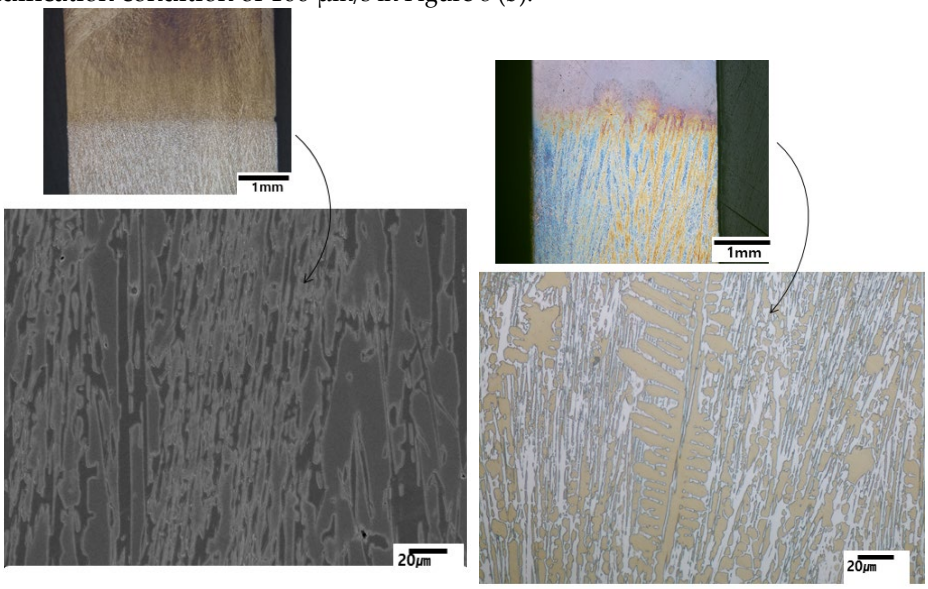

(a) (b)

Figure 8. DSQ micrographs of 2827 alloy: (a) 25 μm/s; (b) 100 μm/s. .

3.4.2. Speckles in a Near Eutectic Alloy

As depicted in Figure 7, speckles are observed on the transverse section to the solidified direction, specifically in specimens where cellular solidification occurs. In the case of 2827 alloy, the speckles appear at solidification rates at or below 50 μm/s, whereas dendrites appear above 100 μm/s. SEM microstructural observation of the speckles in Figure 9 reveals that they have similar constituents to those of the normal area, but have many small white particles and angular M_7C_3 carbides. On the other hand, the normal area has a few small white particles and bigger angular M_7C_3 carbides. The size difference of M_7C_3 carbides indicates the time of solidification that bigger particles formed earlier in the normal area [Figure 9 (c)] than smaller ones in the speckles [Figure 9 (b)]. Therefore, the speckles are formed in the inter-cellular regions of the final freezing area during solidification.

The identification of the different phases present in the material was conducted by transmission electron microscopy (TEM) and selected area diffraction pattern analysis (SADP). As previously mentioned, the big angular particles were confirmed to be M_7C_3 carbide (HCP) [14], while the small white particles were identified as $M_{23}C_6$ carbide, as illustrated in Figures 10 and 11.

The speckle-like feature in Figures 7and 9 was attributed to the precipitation of $M_{23}C_6$ carbide among the big M_7C_3 particles.

 doi:10.20944/preprints202402.0086.v1

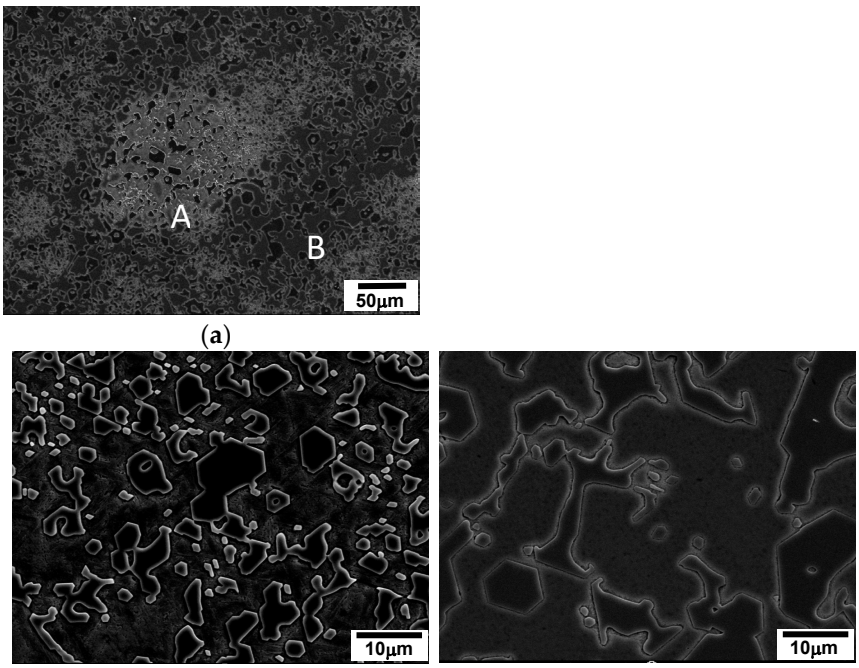

(a) (c) (d)

Figure 9. SEM micrographs transverse to the solidified direction of a near eutectic alloy solidified at 100 μm/s.: (a) SEM micrograph of speckle; (b) 'A' in (a); (c) 'B' in (a).

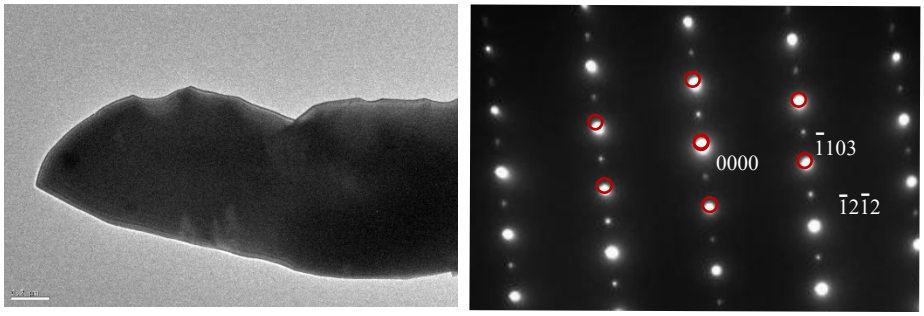

(a) (b)

Figure 10. TEM micrograph and SADP of M_7C_3.

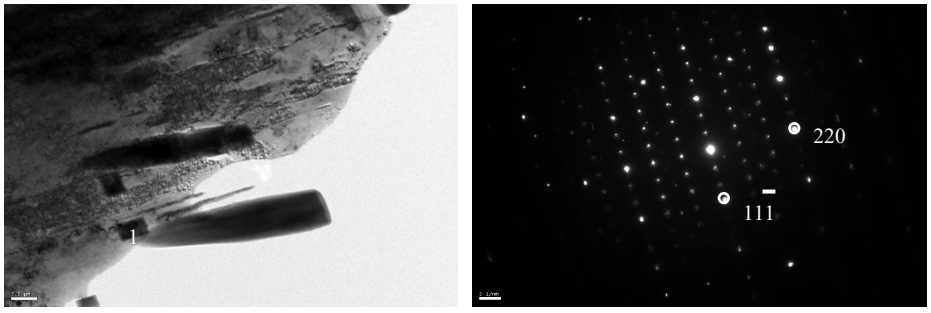

(a) (b)

Figure 11. TEM BF image (a), and SADP of '1' in (a) showing $M_{23}C_6$ (b).

The precipitation of $M_{23}C_6$ carbide in the speckle area was caused by the relatively high concentration of solute elements in the matrix austenite, as reported in reference [12]. The in-situ composite primarily solidified within the cells, which led to the rejection of solute elements to the remaining liquid in the vicinity, then the rejected elements concentrated in the speckles where the final freezing occurred. Consequently, the matrix austenite in the speckle area became supersaturated. During the subsequent slow cooling after directional solidification, the austenite

 doi:10.20944/preprints202402.0086.v1

matrix became destabilized, resulting in the precipitation of secondary carbide $M_{23}C_6$ in the speckle area, as observed in Figure 9 (b). The white speckles depicted in Figure 9 (a) were attributed to the destabilization of the supersaturated austenite [2,8,12,13] that resulted in precipitation of $M_{23}C_6$.

EDS X-ray mapping in Figure 12 shows concentration diffference in speckle area. As mentioned above the speckle area has higher concentartion of Cr and C [concentration of Cr and C is too high to find the difference among the areas but combined mapping of Cr and C in Figure 12 (b) allows the high concentration of both elements).

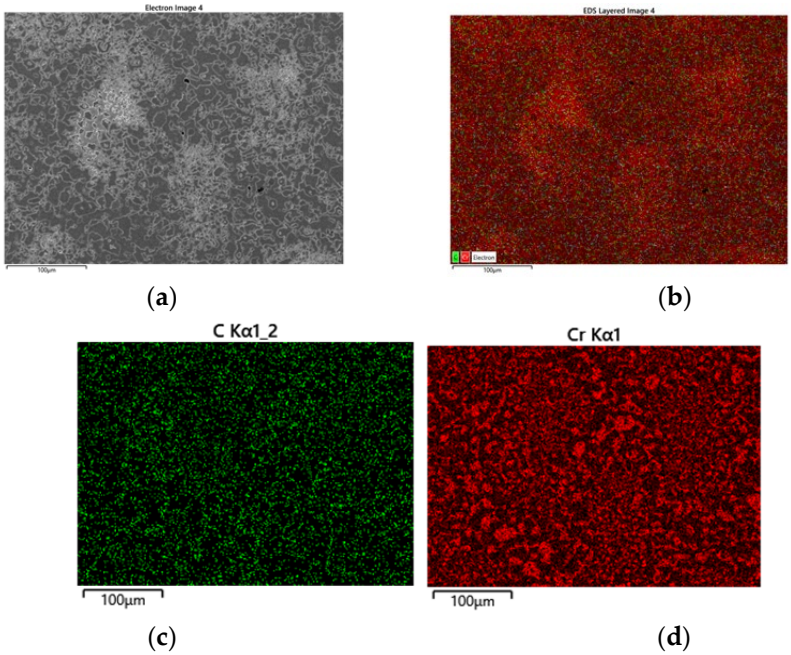

Figure 12. SEM micrographs transverse to the solidified direction of a near eutectic alloy solidified at 100 µm/s.: (a) SEI of speckle; (b) C Kα + Cr Kα mapping; (c) C Kα mapping; (d) Cr Kα mapping.

3.4.3. Microstructural Evolution in Hypoeutectic Alloys

The initial stage of solidification in hypoeutectic alloys involves the formation of austenite. In the case of alloys 2124, 2127 and 2427, primary austenite dendrites formed under all solidification conditions, while a little primary austenite dendrite only appear at high solidification rates (100 µm/s) in the 2827 alloy. Figure 13 shows representative micrographs (taken transverse to the solidification direction) of each alloy, which reveal that the microstructure of the alloy consists of primary austenite dendrites and a M_7C_3/austenite eutectic structure, as expected. As shown in Figure 2, austenite is the leading solidification phase in hypoeutectic alloys. The JMatPro calculated eutectic range was 1290~1285°C (and 1294~1285°C with Thermo-Calc) for these hypoeutectic alloys, as shown in Table 5. Attempts to distinguish the formation of particles in the secondary arm from the M_7C_3 in the eutectic structure using differential scanning calorimetry (DSC) were not successful due to continuous formation and high temperature. However, a few M_7C_3 carbide particles were observed to be embedded in every secondary dendrite arm with the particles located away from the primary austenite dendrite (the "Cross" shaped center of the dendrite) and indicated by white arrows. The location of the M_7C_3 particles in the middle of the secondary arm provides indirect evidence of their formation time. The M_7C_3 particles were enveloped by austenite, which solidified prior to the eutectic (M_7C_3 /austenite) structure of final freezing, and the growth of M_7C_3 on the secondary arms was restricted by the solid austenite, as shown in Figure 13.

Similar to the speckles seen in Figures 7 and 9, white tiny M_7C_3 particles were observed in the interdendritic regions, especially among the secondary arms, as indicated by white circles. Furthermore, the interdendritic regions near the austenite dendrite have a similar feature to the speckles in cellular solidification of a near eutectic alloy. These regions (indicated by circles in Figure 13) contain many small white particles of $M_{23}C_6$, which are believed to be caused by the rejection of solute elements during the progress of austenite dendrite solidification. X-ray mapping of C and Cr

 doi:10.20944/preprints202402.0086.v1

in Figure 14 displays segregation of the elements in the interdendritic region and M_7C_3 carbides that embedded in the secondary dendrite arms. The solute elements became concentrated in the region of final freezing close to the dendrites. The segregated solute, especially Cr and C, in the austenite of the eutectic structure destabilized during the subsequent solid state cooling after solidification. The destabilization of austenite released $M_{23}C_6$ in the vicinity of dendrite arms, as indicated by the circles in Figure 13.

Therefore, the microstructural evolution during the whole cooling process (dendritic solidification and subsequent solid state cooling) of the hypoeutectic alloys is schematically illustrated in Figure 15.

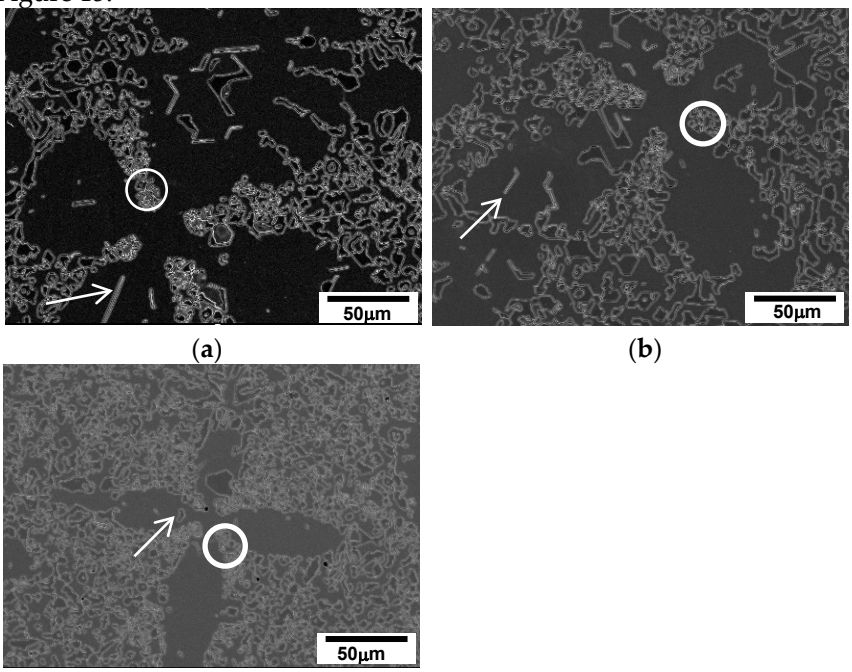

(**a**) (**b**)

(**c**)

Figure 13. SEM micrograph (transverse to DS direction) of each alloy showing M_7C_3 embedded dendrite. (arrow shows M_7C_3 in the secondary arm, circle indicates solute segregated region.): (a) 2127 (at 50 μm/s); (b) 2427 (at 50 μm/s); (c) 2827 (at 100 μm/s).

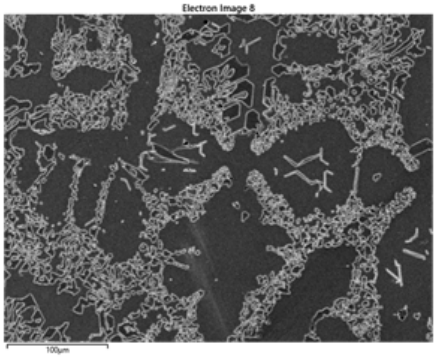

(a)

 doi:10.20944/preprints202402.0086.v1

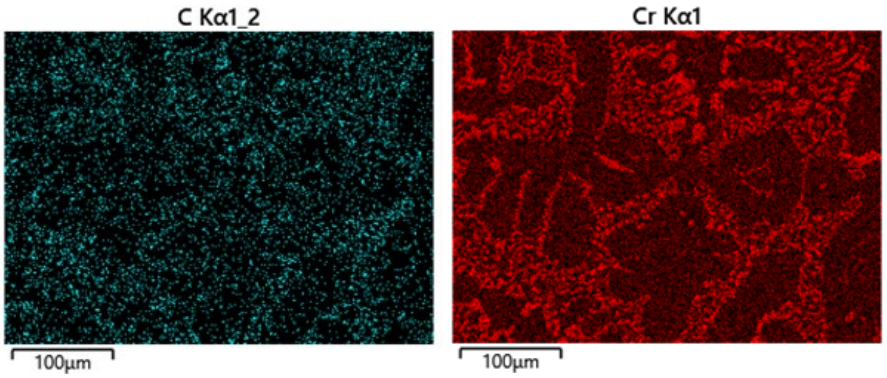

Figure 14. Distribution of alloying elements in 2127 alloy solidified at 50μm/s.: (a) SEI; (b) C Kα; (c) Cr Kα.

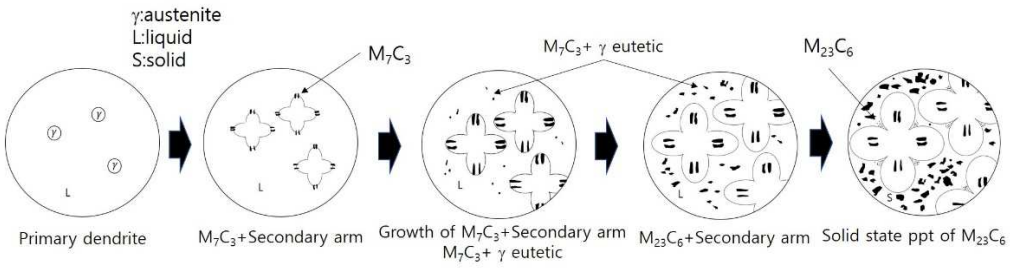

Figure 15. Scheme of microstructural evolution during solidification and subsequent solid state cooling of hypoeutectic alloys.

4. Conclusions

The directional solidification study conducted on high-Cr white irons has led to the following findings:

1. The cooling rate of conventional casting in hypoeutectic alloys (including a near eutectic alloy) was around 10°C/s which was calculated by the casting parameters in directional solidification.

2. Speckle-like feature appeared in a near eutectic alloy at and below 50 μm/s. The size and inter-speckle spacing became smaller with increasing solidification rate in cellular solidification range.

3. The speckles were attributed to the segregation and destabilizing during subsequent cooling after solidification that caused precipitation of $M_{23}C_6$.

4. A near-eutectic alloy displayed a directionally arrayed in-situ composite along the solidified direction. The inter-fibre spacing became finer with increasing solidification rate within cellular solidification condition

5. A few M_7C_3 carbide particles were embedded in the secondary dendrite arms of hypoeutectic alloys. These carbide particles formed prior to the M_7C_3/austenite eutectic structure.

Future work

Mechanical property evaluation of the directionally solidified alloys after heat treatment will be carried out in the future. And phase evolution during thermal treatment will be studied, too.

Acknowledgments: This research was supported by Changwon National University 2023~2024

References

1. Davis, J.R.: Metallurgy and Properties of High-Alloy White Irons, in ASM Specialty Handbook Cast Irons, 1st ed.; ASM International: OH, USA, 1996; pp. 111–122.
2. Oh, J.S., Song Y.G., Choi B.G., Bhamornsut C., Nakkuntod R., Jo C.Y., Lee J.H.: Effect of dendrite fraction on the $M_{23}C_6$ precipitation behavior and the mechanical properties of high-Cr white irons, Metals 2021, 11, 1576.

 doi:10.20944/preprints202402.0086.v1

3. Song, Y.G., Oh J.S., Choi B.G., Jo C.Y., Lee J.H.: Effects of primarily solidified dendrite and thermal treatments on the $M_{23}C_6$ precipitation behavior of high-Cr irons, Metals 2021, 11, 1689.
4. Smith, W.F.: Cast Irons. in Structure and Properties of Engineering Alloys, 1st ed.; Brown, J.V., Maisel, J.W., Eds.; McGraw-Hill: New York, NY, USA, 1981; pp. 322–323.
5. Reed R.: The Superalloys Fundamentals and Applications, Cambridge University Press, 2006, pp. 139-200.
6. Jang D.W., Shin J.H, Kim I.S, Jung I.Y., Jo C.Y., Lee J.H: Effect of Solidification Variables on the Tensile Property of 2.8 wt% C–26 wt% Cr White Iron, Metals 2022, 12, 1416.
7. Smith, W.F. Cast Irons. Structure and Properties of Engineering Alloys, 1st ed.; Brown, J.V., Maisel, J.W., Eds.; McGraw-Hill: New York, NY, USA, 1981; pp. 322–323.
8. Wienmoon, A., Chairuangsri, T., Pierce J.T.H: A microstructural study of destabilized 30wt%Cr-2.3wt%C high-Cr cast iron.ISIJ int. 2004, 44,396-403.
9. Song Y.G., Oh, J.S., Oh D.K., Jo, C.Y., Lee, J.H.: Effect of primary austenite dendrite on the microstructural evolution of high-Cr white irons, The 74th WFC2022, 1-0316
10. McLean, M: Directionally Solidified Materials for High Temperature Service, The Metals Society, 1986, pp 11-54
11. Tiller W.A, Jackson K.A, Rutter J.W., Charlmer B.: Acta Metallurgy, 1953, 1, 428
12. Thrope W.R., Chicco B, Metallurgical Transaction, 1985, 16A, pp 1541~1549.
13. Tabrett C.P.: Microstructure-Property relationships in High Chrome White Irons, PhD Thesis of University of South Australia, 1997.
14. Ma S., Xing J., He Y., Li Y., Huang Z., liu G., Geng Q.: Microstructure and crystallography of M_7C_3 carbide in chrome cast iron, Materials Chemistry and Physics 2015, 11, 65.